Modelling the drained/undrained transition: effect of the measuring method and the boundary conditions

L. Pimienta, J.V.M. Borgomano, J. Fortin, Y. Guéguen

APTARA | GPR | gpr12390 | Dispatch: April 10, 2016 | CE: N/A
Journal | MSP No. | No. of pages: 15 | PE: George

Geophysical Prospecting, 2016 doi: 10.1111/1365-2478.12390

Modelling the drained/undrained transition: effect of the measuring method and the boundary conditions

Q1 L. Pimienta*, J. V. M. Borgomano, J. Fortin and Y. Guéguen

Laboratoire de Géologie de l'ENS - PSL Research University - UMR8538 du CNRS, 75231 Paris, France

Received September 2015, revision accepted February 2016

ABSTRACT

The dependence of fluid-saturated rocks' elastic properties to the measuring frequency is related to fluid-flow phenomena at different scales. In the frequency range of $[10^{-3}, 10^{6}]$ Hz, for fully saturated rocks, two phenomena have been experimentally documented: (i) the drained/undrained transition (i.e., global flow), and (ii) the relaxed/unrelaxed transition (i.e., local flow). When investigating experimentally those effects or comparing different measurements in rocks, one needs to account for both the boundary conditions involved and the method of measurement used. A one-dimensional poroelastic model is presented, which aims at calculating the expected poroelastic response during an experiment. The model is used to test different sets of boundary conditions, as well as the role of the measuring setup, i.e., local (strain gauges) or global (linear variable differential transformer) strain measurement. Four properties are predicted and compared with the measurements, i.e., bulk modulus, bulk attenuation, pseudo-Skempton coefficient, and pore pressure phase shift. For the drained/undrained transition, because fluid pressure may not be homogeneous in the sample, local and global measurements are predicted to differ. Furthermore, the existence of a dead volume at both sample's ends is shown to be important. Due to the existence of the dead volume, an interplay between sample's and dead volumes' storage capacity determines both the magnitudes and the frequency dependence of the dispersion/attenuation measurements. The predicted behaviours are shown to be consistent with the measurements recently reported on very compressible and porous sandstone samples.

INTRODUCTION

Dispersive elastic properties in porous fluid-saturated rocks originate from the presence and mechanical effect of fluid (e.g., Biot 1956; O'Connell and Budiansky 1974). The characteristic frequency of those effects are related to fluid pressure equilibration during the passing of the seismic wave (e.g., O'Connell and Budiansky 1974; Cleary 1978). Two complementary methods have been proposed to investigate experimentally rocks' dispersive elastic properties, i.e., the resonant-bar method and the stress–strain method. The resonant-bar method relies on fixing one side of a sample, applying a small displacement to the other side, and observing the resonance modes of the rock sample (e.g., Winkler and Nur 1979; Bourbie and Zinszner 1985). Depending on the sample's length and diameter, the frequency investigated is of about 10 kHz. However, the method often implies for the sample to be unbounded so that investigating the confining pressure effect is challenging. The stress–strain or sub-resonance method is promising as it allows for measurements over wide frequency ($f \in [10^{-2}; 10^{3}]$ Hz) and pressure ranges (e.g., Subramaniyan *et al.* 2014). Depending on the apparatuses' specificity, different elastic properties can be precisely investigated such as the bulk modulus (e.g., Adelinet *et al.* 2010; David *et al.* 2013; Pimienta, Fortin, and Gueguen 2015a), the shear modulus (e.g., Jackson and Paterson 1987), Young's modulus (e.g., Batzle, Han, and Hofmann 2006; Adam *et al.* 2009; Takei, Fujisawa, and McCarthy 2011;

*E-mail: lucas.xan.pimienta@gmail.com

Tisato and Madonna 2012; Madonna and Tisato 2013; Mikhaltsevitch, Lebedev, and Gurevitch 2014; Pimienta *et al.* 2015b) or Poisson's ratio (Pimienta *et al.* 2016).

When measuring these dispersive properties experimentally, one however needs to properly account for the specific boundary conditions brought by the measuring apparatus and method. For the resonant-bar method or stress–strain experiments under ambient pressure (e.g., Paffenholz and Burkhardt 1989; Lienert and Manghnani 1990; Takei *et al.* 2011), the sample is unbounded so that fluid is allowed to flow laterally. For such experiments, Dunn (1987) has shown that the lateral boundary condition could affect the dispersive properties by creating a lateral fluid flow out of unjacketed samples, i.e., the so-called Biot–Gardner effect. On the contrary, the stress–strain method under confining pressure implies a lateral bounding of the sample by using either epoxy sealing (e.g., Batzle Han, and Hofmann 2006; Adam *et al.* 2006, 2009), copper (e.g., Tisato and Madonna 2012; Madonna and Tisato 2013), or rubber (e.g., Adelinet *et al.* 2010; David *et al.* 2013; Fortin *et al.* 2014; Mikhaltsevitch *et al.* 2014; Pimienta *et al.* 2015a,b, 2016) jacketing. Most of the existing apparatuses have been designed to measure properties on assumed undrained samples, by not allowing for axial fluid flow through the end-platens (e.g., Batzle *et al.* 2006; Tisato and Madonna 2012; Madonna and Tisato 2013; Mikhaltsevitch *et al.* 2014). However, because the saturating procedure might not be optimum with such setups and the drained/undrained transition is of interest, a different setup/methodology has been used at ENS (e.g., Pimienta *et al.* 2015a). The drained conditions have been approached by creating large dead volumes in the drainage system, at the sample's ends, allowing to precisely measure both cause (fluid flow) and consequence (dispersion/attenuation) of the drained/undrained transition (e.g. Pimienta *et al.* 2014a).

To check experimental data against predictions for this drained/undrained transition, a 1D poroelastic model has been derived from solving the pore pressure diffusion equation with different sets of boundary conditions. The technique used for the measurement (i.e., 'local or global) has also been taken into account. The predictions have been compared to measurements on two porous and compliant sandstone samples.

GENERAL 1D POROELASTIC MODEL

Within the framework of linear isotropic poroelastic theory for an homogeneous medium, using the poroelastic relations, the mechanical equilibrium equation, and the mass balance equation, one gets the partial derivative equation satisfied by the pore fluid pressure (p_f) (e.g. Rice and Cleary 1976; Zimmerman 2000; Guéguen and Bouteca 2004:

$$\frac{\partial p_f}{\partial t} - \frac{\kappa B K_d}{\eta\alpha(1-\alpha B)}\nabla^2 p_f = \frac{B K_d}{1-\alpha B}\frac{\partial \epsilon_v}{\partial t}. \quad (1)$$

Where κ, K_d, B, and α are, respectively, the rock's permeability, drained bulk modulus, Skempton coefficient, and Biot coefficient. η is the fluid's intrinsic viscosity, and ϵ_v is the volumetric strain.

Noting that the volumetric strain is $\epsilon_v = K_d^{-1}(P - \alpha p_f)$, equation (1) is a diffusion equation with a source term that depends on the condition of stress solicitation P. Two cases of stress solicitation could be considered. The confining pressure oscillations (e.g., Adelinet *et al.* 2010) can be considered an "*isotropic solicitation*", i.e., a stress solicitation equal in all directions. The uniaxial stress oscillation (e.g. Batzle *et al.* 2006) can be considered a "*deviatoric solicitation.*" Although we focus, in the following, on the "*isotropic solicitation*" case, the case of a "*deviatoric solicitation*" can be shown to give very similar results.

Model derivation: isotropic solicitation

An oscillating confining pressure is applied so that $P(t)$ is a source term that is time dependent. Equation (1) is solved in one dimension (1D model) by assuming p_f to vary as a function of z only. Finally, the equation is rewritten as follows (Zimmerman 2000):

$$\frac{\partial p_f}{\partial t} - \frac{\kappa B K_d}{\eta\alpha}\frac{\partial^2 p_f}{\partial z^2} = B\frac{\partial P}{\partial t}. \quad (2)$$

Noting that the rock's storage coefficient is $S_s = \alpha/(BK_d)$ (Kümpel 1991), the equation is rewritten as follows:

$$\frac{\partial p_f}{\partial t} - \frac{\kappa}{\eta S_s}\frac{\partial^2 p_f}{\partial z^2} = B\frac{\partial P}{\partial t}, \quad (3)$$

which is similar to the heat equation with a heat source.

In case of no source term (i.e., P = const), this equation is that used in the "*oscillating pulse*" method (e.g., Brace, Walsh, and Frangos 1968; Lin 1977; Hsieh *et al.* 1981; Song and Renner 2006, 2007). If $P(t)$ is variable, the source term exists. Here, the applied confining pressure $P(t)$ is supposed to be small variations around a nil value of a sinusoidal form such that $P(t) = \Delta P_0\, e^{i\omega t}$. Accounting for this time dependence, assuming a steady-state solution, and using the method of variables separation with $p_f(z,t) = f(z)e^{i\omega t}$, the partial derivative equation simplifies to

$$f(z) + i\left(\frac{D}{\omega}\right)\frac{d^2}{dz^2}[f(z)] = B\Delta P_0, \quad (4)$$

with $D = \kappa/(S_s\eta)$ being the fluid hydraulic diffusivity in the sample. The equation being simplified to a typical differential equation of second order, steady-state solutions can be found analytically. These are of the form:

$$p_f(z,t) = \left[B\Delta P_0 + p_0^{\pm} e^{\pm(1+i)\sqrt{\frac{\omega}{2D}}z}\right] e^{i\omega t}, \quad (5)$$

with p_0^+ and p_0^- being the two constants that are obtained from the chosen problem's boundary conditions. Knowing $p_f(z,t)$ (equation (5)), the volumetric strain is obtained such that $\epsilon_v(z,t) = K_d^{-1}(P(t) - \alpha p_f(z,t))$.

Solution for undrained and drained boundary conditions

Theoretical derivation

In the undrained condition, fluid is not allowed to flow out of the sample so that

$$\left(\frac{\partial p_f}{\partial z}\right)_{z=L} = \left(\frac{\partial p_f}{\partial z}\right)_{z=0} = 0. \quad (6)$$

The undrained boundary condition leads to a solution of $p_f(t) = B\,P(t)$, i.e., an immediate, position- and frequency-independent response of the pore fluid to the oscillating pressure. Under drained boundary conditions, pore pressure is maintained to the sample upper (i.e., $z = L$) and lower (i.e., $z = 0$) ends so that no overpressure can occur and

$$p_f(0,t) = p_f(L,t) = 0. \quad (7)$$

In the drained boundary condition, the sample's behaviour depends on the frequency of the applied stress oscillation.

Due to the simple drained boundary condition, of nil pore overpressure at both ends, an analytical solution can be found such that

$$p_f(z,t) = B\Delta P_0 e^{i\omega t}\left[1 - \frac{sinh(a(L-z)) + sinh(az)}{sinh(aL)}\right], \quad (8)$$

with the parameter $a = (1+i)\sqrt{\omega/2D}$. As shown from this solution, any value of $p_f(z,t)$ corresponds to the "*local*" fluid overpressure created by the stress oscillation $P(t)$. Finally, a "*local*" volumetric strain can be calculated such that:

$$\epsilon_v(z,t) = \frac{B\Delta P_0}{K_d} e^{i\omega t} \times \left[\left(\frac{1}{B} - \alpha\right) + \alpha\frac{sinh(a(L-z)) + sinh(az)}{sinh(aL)}\right]. \quad (9)$$

Parameter a depends on ω so that, at a given z, both p_f and ϵ_v depend on ω. Moreover, because a is a complex number, p_f and ϵ_v are complex-valued functions. In the following, these are characterized by their amplitude and phase.

Table 1 Parameters values used for the model predictions. The rock parameters and dead volume values are those reported from Pimienta *et al.* (2015a)

Parameter	Estimated value
Sample length	$L = 80$ mm
Sample diameter	$d = 40$ mm
Sample's porosity	$\phi = 7$ %
Sample's drained bulk modulus	$K_d = 14$ GPa
Sample's permeability	$\kappa = 4\,10^{-15}$ m^2
Confining oscillation amplitude	$\Delta P = 0.2$ MPa
Lower Dead volume (1)	$V_1 = 3.4$ mL
Upper Dead volume (2)	$V_2 = 3.2$ mL
Glycerine bulk modulus	$K_{gly} = 4.36$ GPa
Glycerine viscosity	$\eta_{gly} = 1.087$ Pa.s
Lower (1) storage capacity	$S_1 = 7.80\,10^{-4}$ L.GPa^{-1}
Upper (2) storage capacity	$S_2 = 7.34\,10^{-4}$ L.GPa^{-1}
Sample's storage capacity	$S_s = 5.86\,10^{-2}$ GPa^{-1}
Sample's hydraulic diffusivity	$D_{gly} = 6.28\,10^{-5}$ m^2.s^{-1}
Water bulk modulus	$K_{wat} = 2.25$ GPa
Water viscosity	$\eta_{wat} = 0.89\,10^{-3}$ Pa.s
Lower (1) storage capacity	$S_1 = 1.51\,10^{-3}$ L.GPa^{-1}
Upper (2) storage capacity	$S_2 = 1.42\,10^{-3}$ L.GPa^{-1}
Sample's storage capacity	$S_s = 7.36\,10^{-2}$ GPa^{-1}
Sample's hydraulic diffusivity	$D_{wat} = 6.10\,10^{-2}$ m^2.s^{-1}

Discussion of the analytical 1D solution

Values of the different physical parameters. The different parameters used (Table 1) are chosen to be the ones measured experimentally (e.g., Pimienta *et al.* 2015a). The rock's drained bulk modulus varies with confining pressure. Its value is $K_d \sim 14$ GPa at lowest confining pressure (i.e., $P_{eff} = 1$ MPa). The sample's Skempton (B) and Biot–Willis (α) coefficients and storage capacity (S_s) are calculated, assuming the skeleton bulk modulus to be the one of quartz (i.e., $K_{qtz} = 37$ GPa), from usual relations of poroelastic theory (Detournay and Cheng 1993). Finally, the hydraulic diffusivity (D) is directly deduced from the measured sample's permeability (i.e., $\kappa = 4\,10^{-15}$ m^2) and storage capacity (i.e., S_s), and the fluid's viscosity (η).

The behaviours of the fluid-saturated rock depend on two fluid's intrinsic properties. Viscosity affects the hydraulic diffusivity, thus modifying parameter a and introducing a frequency dependence of p_f (equation (5)) and ϵ_v (equation (9)). On the other hand, the fluid's compressibility affects the saturated sample's compressibility, the storage capacity, and the Skempton coefficient B, thus affecting the magnitude of the frequency effect (equations (8) & (9)).

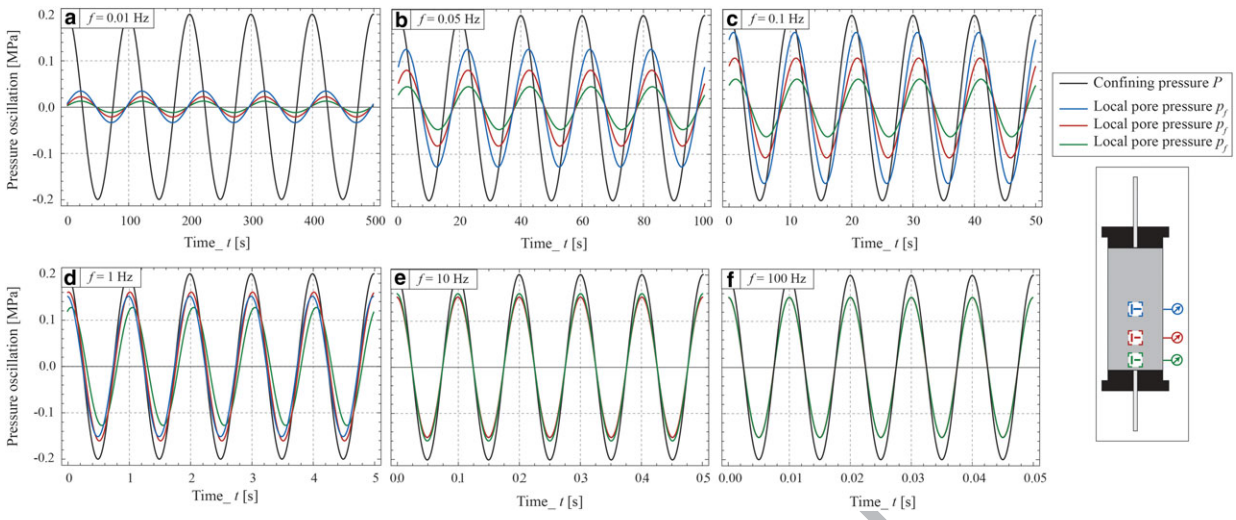

Figure 1 Time dependence of the applied confining pressure oscillations and predicted pore pressure response for different frequencies in the range of $f \in [10^{-2}; 10^{2}]$ Hz. The parameters values are the ones from Table 1 in case of glycerine saturation.

Time dependence. Using the same parameters values as above, the time dependence of p_f for a given oscillating $P(t)$ is reported (Fig. 1). The local p_f is predicted for different frequencies ($f \in [10^{-2}; 10^{2}]$ Hz) and for three sensors' positions using the constants from Table 1 in case of glycerine saturation.

The amplitudes of the induced p_f oscillations increase with increasing frequency, up to $f \sim 10$ Hz (Fig. 1e), where they become independent of frequency. Beyond this frequency, the maximum amplitude of p_f is 0.15 MPa, which consistently relates to case of $B = p_f/P_c = 0.75$. The pore pressure response is initially shifted in time (i.e., phase shift) with respect to $P(t)$, by about $\pi/2$ at lowest frequency of $f = 10^{-2}$ Hz (Fig. 1a). The phase shift decreases, down to zero beyond $f \sim 10$ Hz (Fig. 1e).

The frequency-dependent variation occurs over a very large frequency band, of about $f \in [10^{-2}; 10^{1}]$ Hz. Owing to the boundary conditions, a large dependence to the position of the strain (or pore pressure) sensor is observed. This point is further investigated below.

Spatial dependence. The position (z) dependence of both amplitude and phase of the "*local*" pore pressure (i.e., p_f) and strain (i.e., ϵ_v) is reported in Fig. 2. The properties are calculated for different frequencies of the applied P in the range of $f \in [10^{-2}; 10^{2}]$ Hz. Consistently, p_f amplitudes are low and ϵ_v are high (i.e., low bulk modulus), at lowest f. For the fluid pressure p_f, amplitude and phase show a similar monotonous behaviour. As frequency increases, the amplitude (Fig. 2a) increases, and the phase (Fig. 2b) decreases. The volumetric strain ϵ_v amplitude is also monotonous (Fig. 2c), but the phase is not (Fig. 2d). At low frequency, the amplitude decreases and phase increases as frequency increases. However, there exists a critical frequency (i.e., $f \sim 0.1$ Hz) beyond which the strain phase decreases when frequency keeps increasing.

At low f, the largest amplitude is observed at the sample's centre. As frequency increases, almost all of the sample shows the same response. Because of the symmetry chosen for the boundary conditions, the variations are symmetric with respect to the sample's center. Note that, for each position, it exists a frequency at which the signal (e.g., p_f or ϵ_v) exceeds the maximum value obtained at highest frequency. This observation was also reported by Dunn (1987) and Wang (2000).

"Local" versus "Global" predictions. As in (Pimienta *et al.* 2015a), a local pseudo-Skempton coefficient B^* is defined. Similarly, a local pseudo-bulk modulus K^* may be directly deduced from the complex volumetric strain:

$$B^*(z,\omega) = \frac{p_f(z,\omega)}{P(\omega)}, \quad \textit{and} \quad K^*(z,\omega) = -\frac{P(\omega)}{\epsilon_v(z,\omega)}. \tag{10}$$

The parameters depend on the intrinsic properties (i.e., B and K) of a given rock sample for the specific conditions of the experiment. However, because both parameters bear a dynamic information, those are addressed as "*pseudo*"-properties. The locally calculated K^* and B^* can be averaged over the sample's length L to get global (or volume-averaged) properties of the rock (i.e., K_g and B_g) such that:

$$B_g(\omega) = \frac{\frac{1}{L}\int_0^L p_f(z,\omega)\,dz}{P(\omega)}, \text{ and } K_g(\omega) = -\frac{P(\omega)}{\frac{1}{L}\int_0^L \epsilon_v(z,\omega)\,dz}. \tag{11}$$

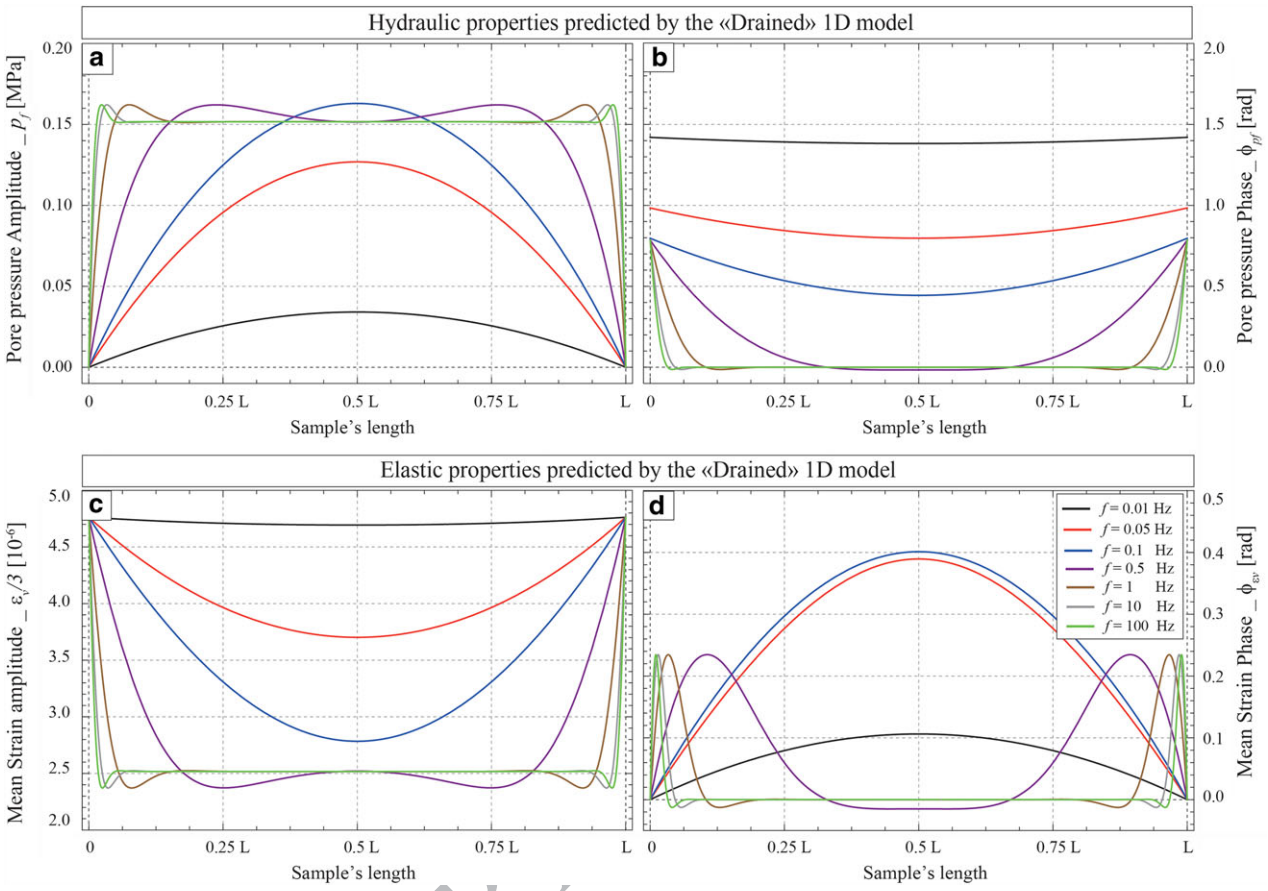

Figure 2 Position dependence of the predicted (a-b) pore pressure and (c-d) mean strain (i.e., $\epsilon_v/3$) response to the applied confining pressure oscillations for different frequencies in the range of $f \in [10^{-2}; 10^{2}]$ Hz. Both signals' amplitudes and phases are investigated. The properties for the prediction are the ones from Table 1 in case of glycerine saturation.

Both B_g and K_g also bear a dynamic information and are "*pseudo*"-properties.

Again, the "*local*" and "*global*" predictions can be characterised by their amplitudes (e.g., $\|B^*\|$ and $\|K^*\|$) and phases (e.g., ϕ_{B^*} and ϕ_{K^*}). The amplitudes are related to the material constants, i.e., K_d and B. The phase ϕ_{B^*} describes the shift in fluid pressure as compared to the applied confining pressure, and depends on the sample hydraulic diffusivity. The phase ϕ_{K^*} is the phase shift between the applied confining pressure and volumetric strain, and $Tan(\phi_{K^*})$ is the bulk modulus attenuation (i.e., Q_K^{-1}).

Both "*local*" and "*global*" hydraulic (Figs. 3a and 3b) and solid (Figs. 3c and 3d) responses to the applied confining pressure oscillation are predicted as a function of frequency using the parameters from Table 1. Three positions have been chosen along the sample's length at $z = [L/2; L/4; L/10]$. Overall, (i) $\|B^*\|$ (Fig. 3a) and $\|K^*\|$ (Fig. 3c) show a consistent increase from drained to undrained domain, (ii) the phase shift ϕ_{B^*} shows large decrease with frequency, from $\pi/2$ down to zero, and (iii) a large Q_K^{-1} peak is observed. For all properties, owing to the water intrinsic viscosity, the transition is shifted to higher frequency in comparison to the glycerine saturation.

Consistently, the "*local*" predictions show no frequency dependence at either very high (i.e., $f > 10^2$ Hz for glycerine) or very low (i.e., $f < 10^{-3}$ Hz) frequencies, i.e., corresponding to the undrained and drained regimes, respectively. In the characteristic frequency domain of the drained/undrained transition, clear dependence to the position is predicted for all properties.

"Experimentally undrained" boundary condition

The two typical boundary conditions most often considered are the "*drained*" (Fig. 4a) and "*undrained*" (Fig. 4b) conditions (e.g., Dunn 1986, 1987). They correspond to the

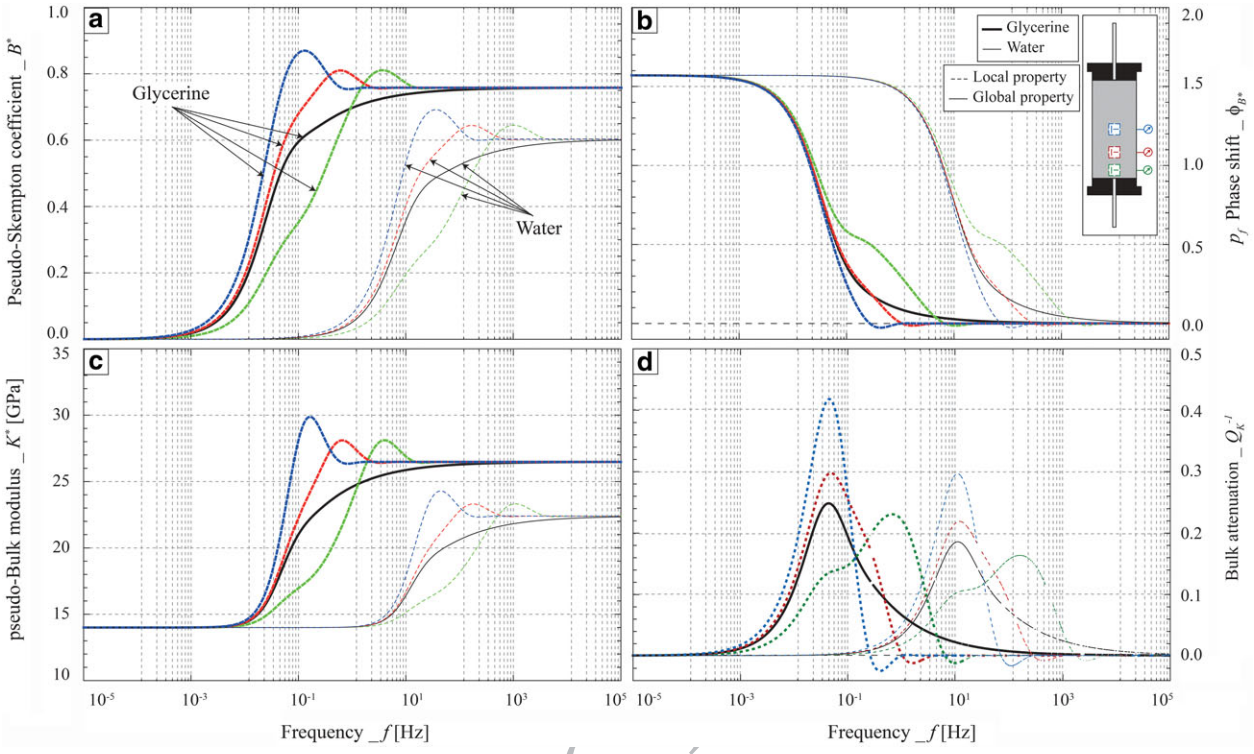

Figure 3 Predicted drained to undrained transition of the frequency-dependent (a-b) hydraulic and (c-d) elastic properties of a representative sandstone sample saturated by water (i.e., thin curves) or glycerine (i.e., thick curves). Both "*local*" (i.e. dashed colour curves) and "*global*" (i.e. continuous black curves) predictions are compared. The two cases of water and glycerine saturating conditions are tested.

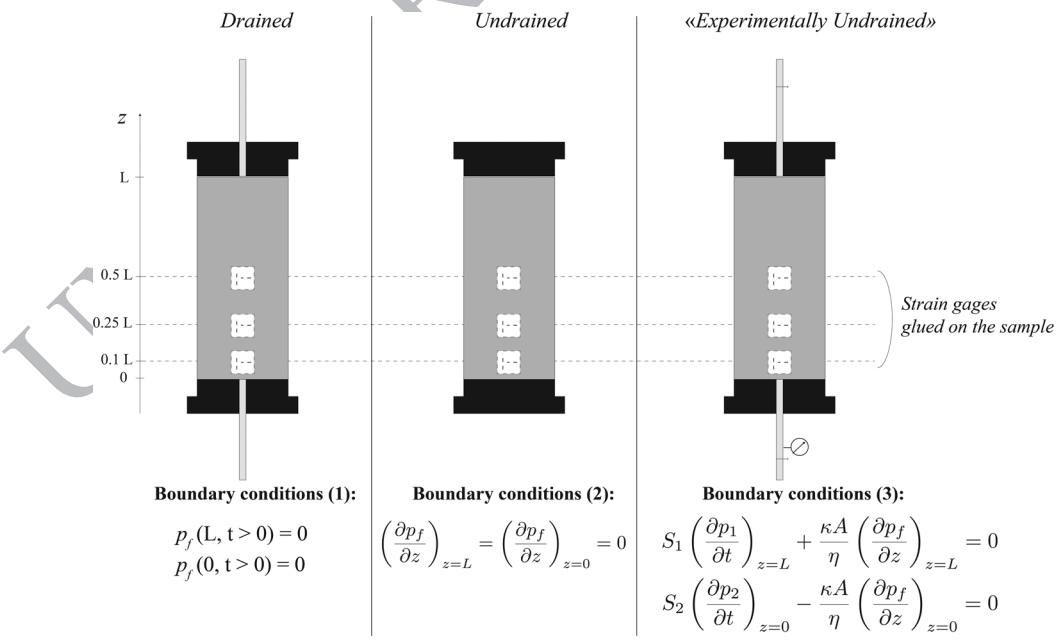

Figure 4 Schematic view of the sample associated with the three possible boundary conditions. The theoretical (a) "*drained*" and (b) "*undrained*" boundary conditions are complemented with the more realistic (c) "*experimentally undrained*" boundary condition, which in fact combines the two theoretical ones.

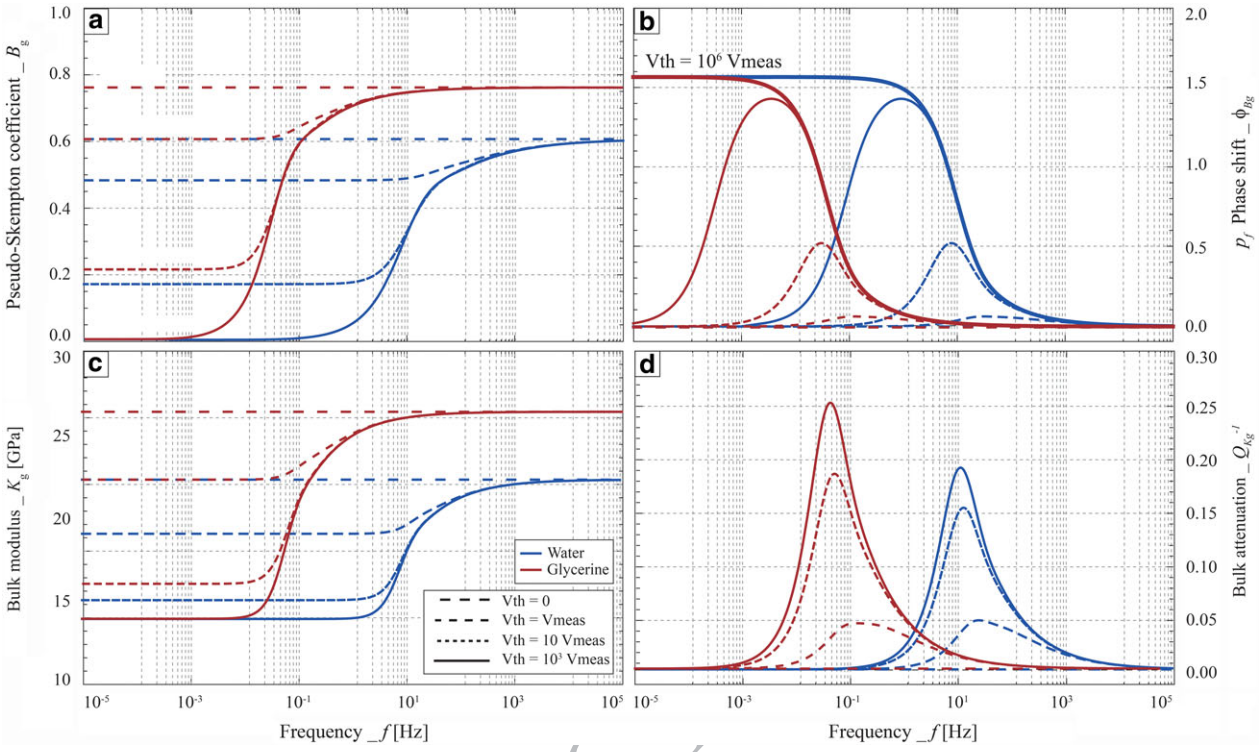

Figure 5 Predicted frequency dependence of the (a-b) hydraulic and (c-d) elastic response of the fluid-saturated sandstone sample. The "*global*" prediction are reported, i.e., the response averaged over the sample's length.

extremal cases of fluid either fully blocked or fully unblocked in the sample. A third boundary condition should be addressed, which combines the purely "*drained*" and "*undrained*" conditions: the "*experimentally undrained*" condition described below (Fig. 4c). This last condition is the most realistic one because: (i) it is often difficult to attain experimentally the purely "*undrained*" (e.g., Ghabezloo and Sulem 2009) experimental conditions, and (ii) it has been shown (e.g., Pimienta *et al.* 2015a) that measuring precisely attenuations under purely "*drained*" conditions was technically challenging.

Role of the dead volumes

The "*experimentally undrained*" boundary condition consists in an undrained system not only constituted of the sample but also of a dead volume at both sample's upper and lower ends. Such boundary condition is also that considered for the "*oscillating pulse*" technique (e.g., Brace *et al.* 1968; Lin 1977; Hsieh *et al.* 1981; Song and Renner 2006, 2007). Fluid mass continuity at both ends of the sample is imposed, i.e., the change of fluid mass in the sample equals the fluid mass change in the dead volume. Following earlier studies, these boundary conditions are found to be (Brace *et al.* 1968; Lin 1977):

$$\begin{cases} S_1 \left(\dfrac{\partial p_1}{\partial t}\right)_{z=L} + \dfrac{\kappa A}{\eta}\left(\dfrac{\partial p_f}{\partial z}\right)_{z=L} = 0 \\ S_2 \left(\dfrac{\partial p_2}{\partial t}\right)_{z=0} - \dfrac{\kappa A}{\eta}\left(\dfrac{\partial p_f}{\partial z}\right)_{z=0} = 0, \end{cases} \tag{12}$$

where S_1 and S_2 are respectively the storage capacities of downstream and upstream dead volumes, and $p_1 = p_f(0,t)$ and $p_2 = p_f(L,t)$ are the fluid pressures in the downstream and upstream dead volumes, respectively. A is the sample's cross-sectional area through which Darcy flow takes place.

From Equation (12), the dead volumes contribute through their overall storage capacity. Due to the very low pressure variations applied (i.e., $\Delta P = 0.2$ MPa), leading to even lower pore pressure variations, the tubing's compressibility can consistently be neglected so that only the compressibility of the fluid in the dead volume needs to be accounted for. Knowing the values of lower (i.e., V_1) and upper (i.e., V_2) dead volumes and the fluid bulk modulus K_f, S_1 and S_2 are obtained such that $S_{1,2} = V_{1,2}\,K_f^{-1}$. The sample's storage capacity is reached from the theoretical relations (e.g., Kümpel 1991). All required parameters are listed in Table 1.

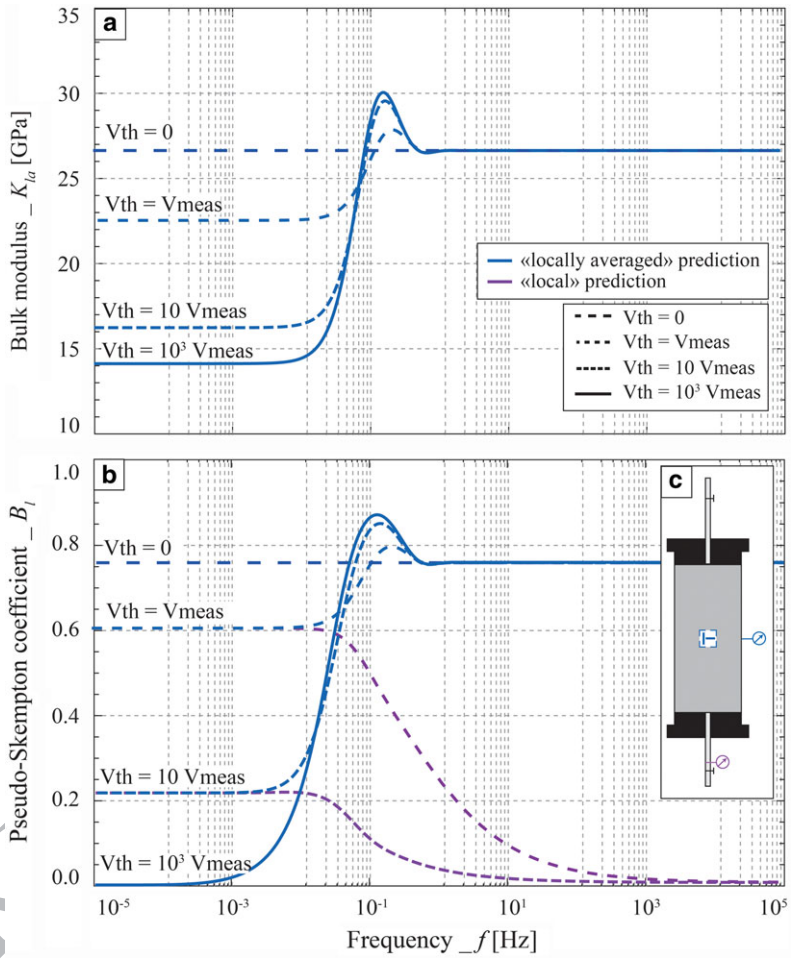

Figure 6 Predicted frequency dependence of K_{la}, B_{la}, and B_l for the glycerine-saturated sandstone sample. Different values of dead volume V_{th} are chosen, starting from zero, up to a value a thousand times higher than the one measured ($V_{th} = V_{meas}$).

The general solution can be obtained for example by solving equation (5) using the ***Mathematica*** software. Solving $p_f(z,t)$ for this realistic set of boundary conditions would lead to a complex solution that cannot be reported in a simple formula. However, a simple analytical solution is found if $S_1 = S_2$ (i.e., $V_1 \sim V_2$). In the case of the setup used by Pimienta *et al.* (2015a), such assumption can consistently be made as $V_1 = 3.4$ mL and $V_2 = 3.2$ mL. Using this assumption, one gets the system:

$$\begin{cases} p_0^-(b+1) = p_0^+(b-1) - B\Delta P_0, \\ p_0^+(b+1)e^{aL} = p_0^-(b-1)e^{-aL} - B\Delta P_0, \end{cases} \tag{13}$$

with $b = (1-i)A(S_s/S)\sqrt{2D/\omega}$, and $S = S_1 + S_2$ being the dead volume storage capacity. Subtracting the two above equations, one obtains:

$$(p_0^- - p_0^+ e^{aL})\left[(1+b) - \frac{(1-b)}{e^{aL}}\right] = 0. \tag{14}$$

This implies that $p_0^- = p_0^+ e^{aL}$ because a, b, and L have fixed values so that the second term differs from zero. Further solving the system (13) and replacing the constants in equation (5) leads to the general solution:

$$p_f(z,t) = B\Delta P_0 e^{i\omega t}\left[1 - \frac{cosh(a(\frac{L}{2} - z))}{bsinh\left(a\frac{L}{2}\right) + cosh\left(a\frac{L}{2}\right)}\right], \tag{15}$$

Interestingly, recalling that $a \propto \sqrt{\omega}$ and $b \propto (1/\sqrt{\omega})$, the limiting quasi-static case (i.e., zero frequency) can be reached from equation (15) using the Taylor expansion of *cosh* and *sinh* to the first order in ω. Further noting that $a\,b\,(L/2) = (2AS_s/S)(L/2) = V_s(S_s/S)$, the limiting quasi-static case is:

$$\left(\frac{p_f(z,t)}{P(t)}\right)_{\omega=0} = B_0 = B\frac{V_s S_s}{V_s S_s + S}. \tag{16}$$

where $V_s = AL$ is the sample's total volume, and B is the Skempton coefficient. The general result (i.e., with $V_1 \neq V_2$) can further be found from introducing $S = S_1 + S_2$ in equation (16). This solution under quasi-static conditions is

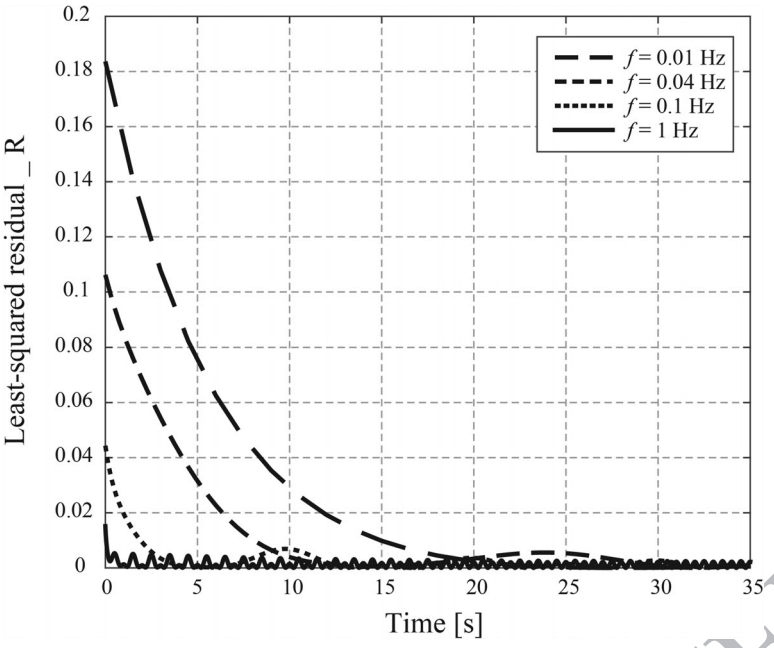

Figure 7 Comparison of the differences quantified by R (sum of squared residuals through the sample's length), between the analytical and the numerical solutions of the pore-fluid pressure oscillations at different frequencies. The parameters used are the ones of Table 1 in the case of glycerine saturation, under drained boundary conditions.

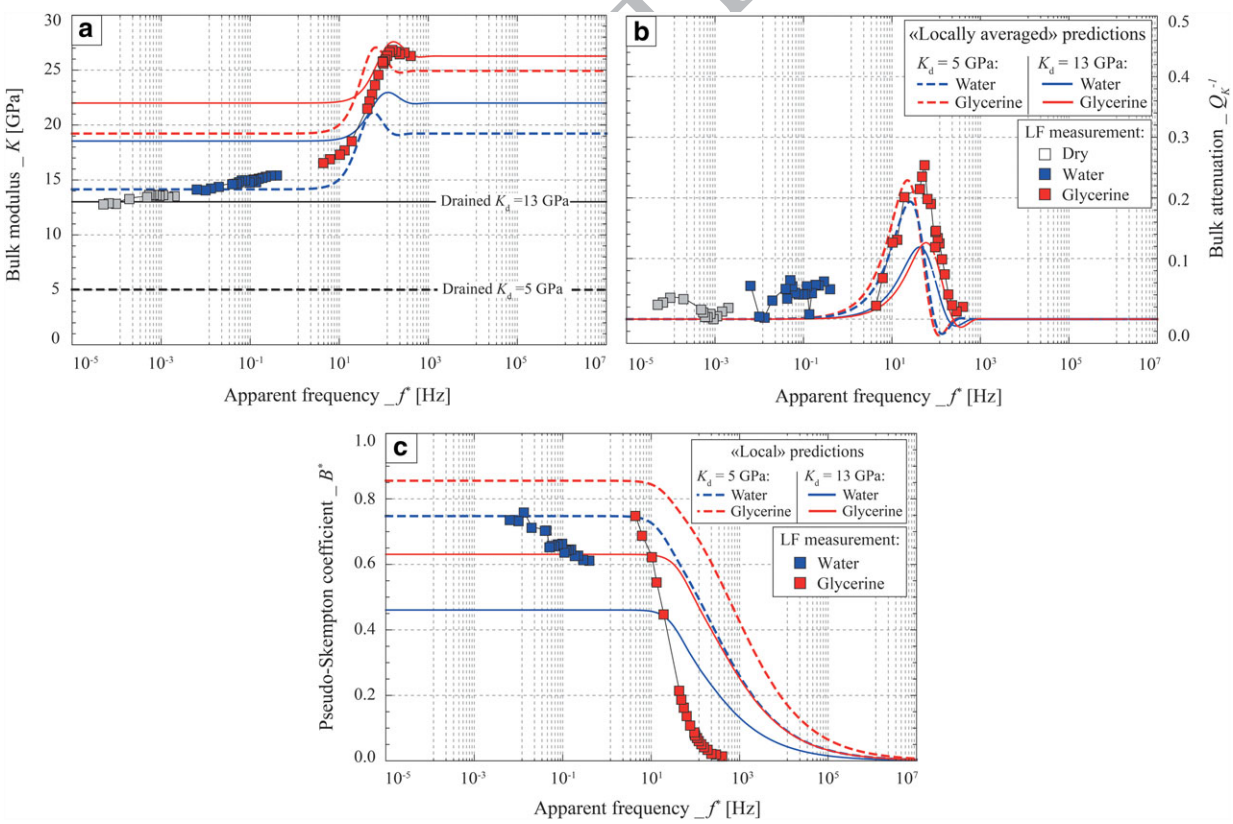

Figure 8 Comparison between predicted and measured frequency-dependent properties for a 7%-porosity Fontainebleau sandstone. The measured (a) bulk modulus and (b) attenuation have been measured locally at the sample centre, and (c) the pseudo-Skempton coefficient has been measured in the dead volume. These data are compared with the corresponding model predictions with "*experimentally undrained*" boundary conditions. Two values of K_d of 5 GPa (i.e., dashed curves) and 13 GPa are chosen for the predictions.

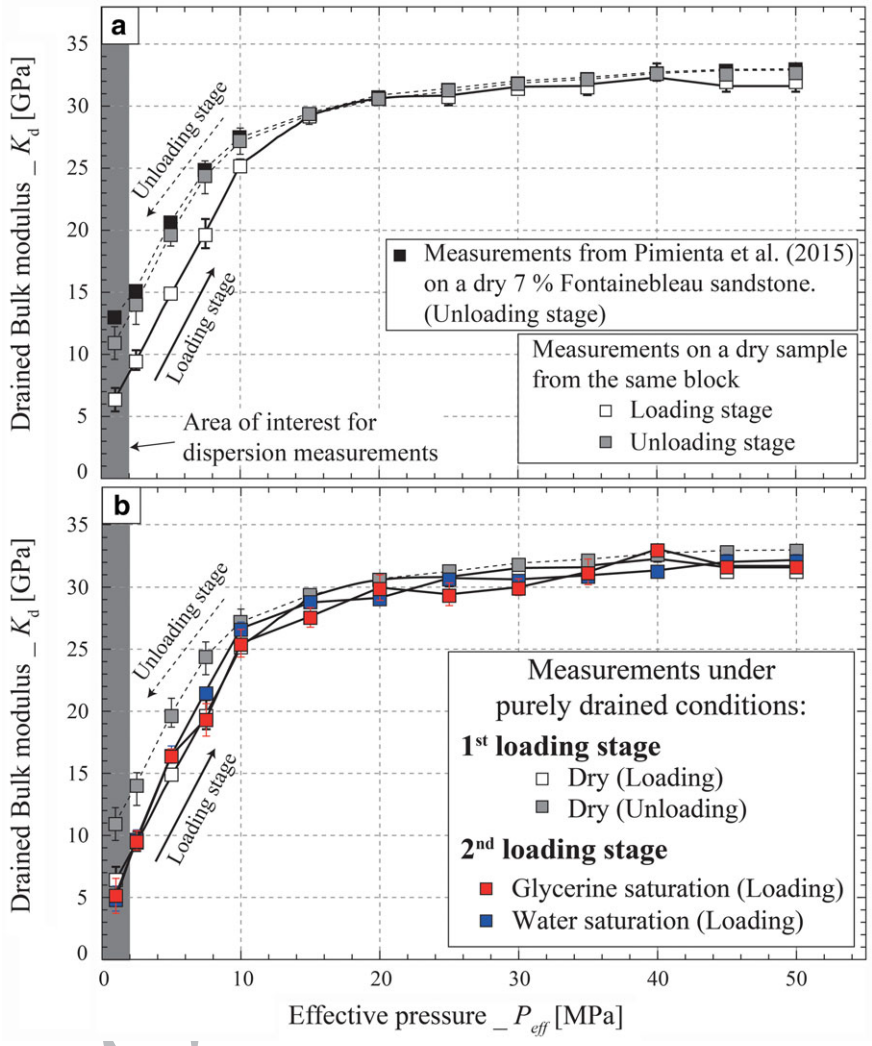

Figure 9 (a) Measured dry bulk modulus as a function of effective pressure for two Fontainebleau sandstone samples of 7% porosity. K_d is measured under both loading and unloading stages. (b) Measured drained bulk modulus under loading stage for the three fluid-saturated conditions. The first "*loading stage*" is the one under dry conditions, where the sample is measured under loading then unloading. The second "*loading stage*" comes after. During this stage, the rock is fully-saturated by glycerine and then water. For each saturating fluid, the rock is measured under loading only. Note the greyish area corresponding to the effective pressure at which the frequency effects are investigated.

consistent with the results from Ghabezloo and Sulem (2010), and implies that the measured B_0 is equal to the Skempton coefficient B only if $S_1 = S_2 = 0$ (i.e., $V_1 = V_2 = 0$). As shown by previous authors (e.g., Ghabezloo and Sulem 2010), the idealistic condition of $V_1 = V_2 = 0$ can seldomly be reached experimentally so that the above result needs to be applied.

"Global" predictions

In order to apply the present model in a simple way to the experiment reported by Pimienta *et al.* (2015a), the two dead volumes are assumed equal (i.e., $V_1 = V_2$) so that the total dead volume is $V_{meas} = 6.6$mL. As a consequence, following equation (15), the problem is symmetric with respect to $L/2$. The model's "*global*" predictions, averaged over the entire sample's length, are first investigated. They are noted K_g and $Q_{K_g}^{-1}$ for the predicted elastic response, and B_g and ϕ_{B_g} for the hydraulic response. The frequency-dependent hydraulic (Figs. 5a and 5b) and elastic (Figs. 5c and 5d) model's responses are predicted using the parameters from table (1). In order to check the sensitivity to the total dead volume value, a theoretical dead volume V_{th} is introduced. This parameter is varied from V_{meas} to values of 0, 10 V_{meas} and 10^3 V_{meas}, and even to 10^6 V_{meas} for the p_f phase shift.

A zero dead volume (i.e., $V_{th} = 0$) corresponds to the "*undrained*" boundary condition. In that case, for all frequencies: (i) the predicted B_g equals Skempton coefficient B, (ii) there is no phase shift for p_f, and (iii) $K_g = K_{ud}$ (i.e., undrained bulk modulus) and $Q_{Kg}^{-1} = 0$. A very high dead volume (i.e., $V_{th} \geq 10^3\, V_{meas}$) corresponds to the "*drained*" boundary condition (Fig. 3). In that case: (i) at frequencies low enough, there is no Skempton coefficient (i.e., $B_g = 0$) and $K_g = K_d$, and (ii) a critical frequency f_c exists at which the regime switches from "*drained*" to "*undrained*". At f_c, a maximum in Q_{Kg}^{-1} is predicted.

The intermediate dead volumes (i.e., $V_{th} = V_{meas}$ and $V_{th} = 10\, V_{meas}$) lead to an intermediate case scenario, in between "*drained*" and "*undrained*" boundary conditions. In that final case, at frequencies low enough: (i) B_g exists but is below B (Fig. 5a), (ii) $K_d < K_g < K_{ud}$ (Fig. 5c), and (iii) dependence to the fluid bulk modulus K_f is observed (Fig. 5a, c, d). Moreover, as for the "*drained*" boundary condition, a critical frequency f_c exists at which a maximum in Q_{Kg}^{-1} is predicted (Fig. 5d). Beyond f_c, B_g and K_g reach, respectively, the undrained B and K_{ud}. As V_{th} decreases, the magnitudes of the variations between drained and undrained regime decrease, and, consistently, the maximum in Q_{Kg}^{-1} decreases. Note finally that, as V_{th} decreases, the value for f_c slightly increases.

"local" and "locally averaged" predictions

The "*locally averaged*" predictions can be calculated by averaging over the strain gauge length (i.e., 6 mm) at the sample's center, i.e., $(L/2) \pm 3$ mm. They are noted K_{la} and B_{la}. In case of the pseudo-Skempton coefficient, a second "*local*" prediction B_l is investigated at a position infinitely near to the boundary, so that the frequency-dependent variations measured experimentally in the dead volume (Pimienta *et al.* 2015a) can be approached. The frequency-dependent variations predicted for K_{la}, B_{la}, and B_l under glycerine saturation are reported (Figs. 6a and 6b).

A strong effect of the dead volume is again predicted. At lowest and highest frequencies, the values equal the ones of the "*global*" predictions. However, a sharper increase is predicted for the transition of K_{la} and B_{la}, which is similar to a characteristic transition of a viscoelastic Zener-like material. Interestingly, B_l decreases as frequency increases (Fig. 6b). It indicates that fluid can less and less flow out of the sample as frequency increases, i.e., the sample becomes undrained.

Transient regime and numerical solution

The analytical solution obtained (Eq. 8) corresponds to the steady-state response of the pore pressure to an oscillating confining pressure. However, considering the time $t_0 = 0$ to be the beginning of the oscillation, a transition exists between the initial static state (at $t_0 < 0$) and the steady-state oscillation. In order to investigate this transient regime, a 1D finite-difference scheme, with imposed initial conditions (i.e., $P(t_0) = 0$, and $p_f(z, t_0) = 0$), is used to solve numerically the diffusion equation (Eq. 1). A first-order backward difference for time and a second-order central difference for space has been chosen. The grid used is uniform, with a constant mesh spacing of Δz for space and a constant time increment of Δt. The boundary conditions tested correspond to the drained regime, which are taken into account with the two Dirichlet boundary conditions (i.e., $p_f(0, t) = 0$, and $p_f(L, t) = 0$) at both ends of the space grid. For the initial conditions, the pore pressure is zero throughout all the sample (i.e., $p_f(z, 0) = 0$).

A parameter R is introduced to compare analytical and numerical solutions, respectively, p_f and $\widetilde{p_f}$. R is defined as the sum of the squared residuals through the sample's length, i.e., of the difference between analytic and numerical solutions for a particular position $z_i = i\,\Delta z$. For each time step $t_j = j\,\Delta t$, R is defined as:

$$R(j) = \sum_i \left| p_f(z_i, t_j) - \widetilde{p_f}_i^{\,j} \right|^2. \quad (17)$$

The solutions are compared as a function of time for different oscillating frequencies (Fig. 7). For simplicity, the drained 1D model (Fig. 4a) is used.

For each frequency, the sum of squared residuals R is maximum at the initial conditions ($t = 0$), then decreases with time to reach a steady state where the difference between the analytical and numerical solutions is negligible. The transient behaviour observed for R relates to the transient behaviour accounted for in the numerical solution. As frequency increases, R decreases. The duration of this transient behaviour is always less than one oscillation period for any frequency. Therefore, the analytical solution can be considered valid after one oscillation.

COMPARISON WITH THE MEASUREMENTS

The above model predictions are used to discuss the measurements on two sandstone (i.e., Fontainebleau and Berea) samples. The dead volume is set to 6.6 mL, with $V_1 = V_2$. The other required parameters are: (i) the drained (i.e., dry) bulk

modulus; (ii) the sample's porosity and permeability; and (iii) the fluid's viscosity. All these parameters are known. Finally, Biot–Willis, Skempton, and storage coefficients are derived from the poroelastic relations. The skeleton bulk modulus is taken as 37 GPa for both rocks.

The model's predictions are calculated for the appropriate experimental conditions, i.e., what has been defined as the "*experimentally undrained*" boundary condition. Moreover, the strains have been recorded at the sample's centre, and the pore pressure measurement has been taken in the dead volume. Accordingly, the "*locally averaged*" K_{la} and $Q_{K_{la}}^{-1}$ are predicted at the sample centre, and the "*local*" B_l is calculated very close to the dead volume. In the following, an apparent frequency parameter (i.e., $f^* = f\,(\eta/\eta_0)$, with $\eta_0 = 10^{-3}$ Pa.s) is introduced to account for the fluid's viscosity.

Results for a Fontainebleau sandstone

"Experimentally undrained" boundary conditions

The data are those of Pimienta *et al.* (2015a), measured on a Fontainebleau sandstone sample of 7% porosity. All parameters for the predictions are the ones of Table 1. Measurements at an effective pressure of $P_{eff} = 1$ MPa and model's predictions are compared as a function of apparent frequency f^* (Fig. 8). Three properties are investigated: (i) bulk modulus K (Fig. 8a), (ii) bulk modulus dissipation Q_K^{-1} (Fig. 8b), and (iii) pseudo-Skempton coefficient B^* (Fig. 8c). The model's predictions are calculated for two extreme values of K_d, of 5 GPa and 13 GPa, respectively.

Note first that the frequency range for the transition predicted by the model is very consistent with the measurements and occurs at $f^* \sim 10$ Hz. A strong effect of the "*experimentally undrained*" boundary condition is predicted so that, for a K_d of 13 GPa, the values of (i) K_{la} at lowest f^* overestimates the measurements (Fig. 8a), (ii) $Q_{K_{la}}^{-1}$ underestimates the measured Q_K^{-1} peak (Fig. 8b), and (iii) B_l at lowest f^* underestimates the values of B^* measured (Fig. 8c).

Comparisons between measurements and model predictions thus add up and imply that measurements under liquid saturation relate to an initial K_d much lower than 13 GPa. A second prediction is thus tested with $K_d = 5$ GPa. The predicted properties are consistent with the measurements under fluid-saturated conditions. For all properties, under water saturation, a good fit is obtained between measurements and model predictions. Under glycerine saturation, both K_{la} (Fig. 8a) and B_l (Fig. 8b) gain in consistency with the measurements. Moreover, the peak in $Q_{K_{la}}^{-1}$ is at about 0.25 (Fig. 8c), which is precisely what has been measured.

Role of the confining cycle

As the measured value under dry conditions is of 13GPa – 14 GPa (Fig. 8a), it implies that K_d is lower under fluid-saturated conditions. Because glycerine is not a polar fluid and this sample is well cemented, a possible fluid-related elastic weakening (e.g., Pimienta *et al.* 2014b) may be ruled out. Noting that this K_d value was measured after cycling the sample up to high pressure and back (Pimienta *et al.* 2015a), the effect of cycling is tested on a sample from the same block (Fig. 9a).

For this rock sample, at pressures lower than $P_{eff} = 10$ MPa, the K_d values after the loading stage are higher than the ones before (Fig. 9a). For the particular case of $P_{eff} = 1$ MPa, the cycling introduces a variation from $K_d = 5$ GPa (before cycling) to $K_d = 13$ GPa (after cycling). After unloading the sample, glycerine and then water are injected in the sample, and the drained bulk modulus is measured again under purely drained boundary conditions (Fig. 9b). Under both water and glycerine saturation, the value at 1 MPa is of 5 GPa, which equals the value measured during the (first) loading stage under dry conditions. This is precisely this value of $K_d = 5$ GPa that has been chosen for the 1D model predictions (Fig. 8), under fluid-saturated conditions. It implies that, for this sample, and this experimental protocol, the hysteresis seems to disappear when measuring again (after cycling) under fluid saturation. This hysteresis effect under dry conditions may be caused by grain–grain or cracks internal friction (e.g., David *et al.* 2012) that indeed largely reduces when fluid is present and pressurized.

Results for a Berea sandstone

Berea sandstone

Berea sandstone has been extensively used in experimental rock physics (e.g., Sayers, Van Munster, and King 1990; Seipold, Mueller, and Tuisku 1998) as a reference rock. As detailed by Pimienta *et al.* (2014c), it is characterized by: (i) a porosity in the range of $\phi \in [17; 22]$%, (ii) a permeability in the range of $\kappa \in [1; 10^3]$ mD, (iii) a variable mineralogy, with mean (over 19 Berea sandstone samples) quartz and clay contents of ~ 75% and ~ 11% respectively. As shown through microstructural observation (e.g., Prasad and Manghnani 1997), Berea sandstone's pore network is composed of: (i) relatively equant pores, and (ii) intergranular thin

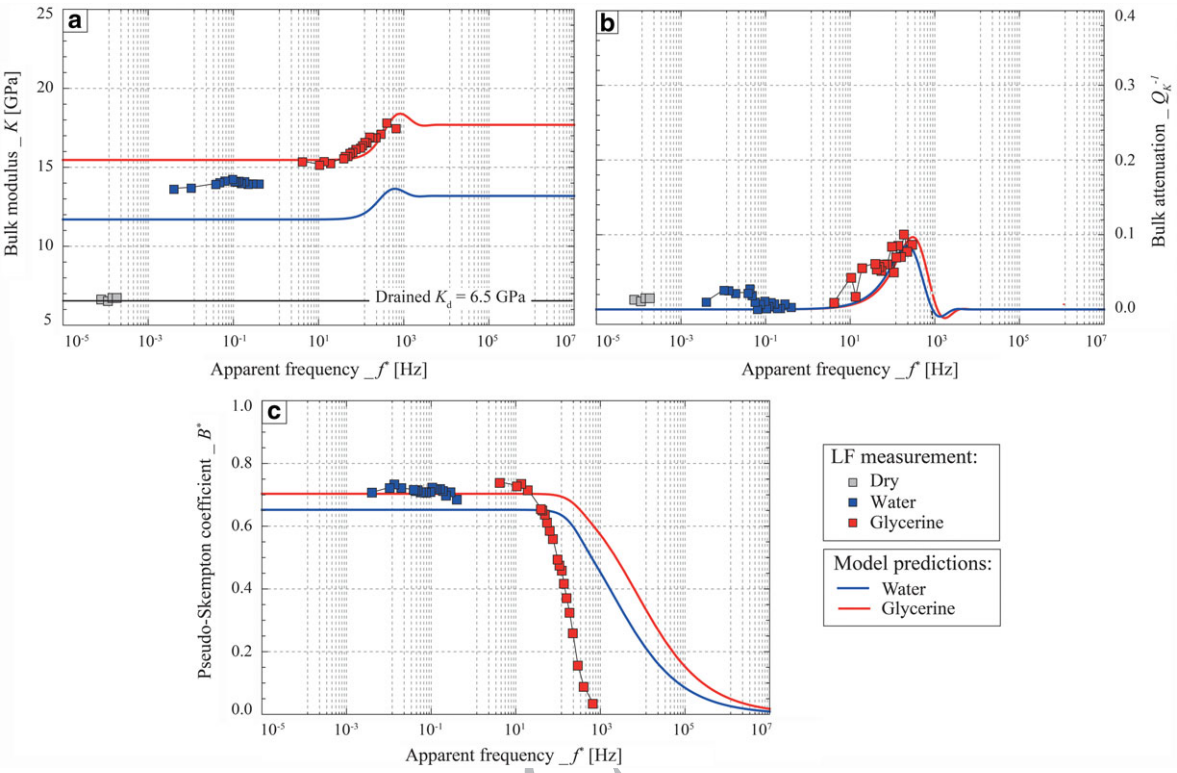

Figure 10 Comparison between predicted and measured (a-b) elastic and (c) hydraulic properties as a function of apparent frequency for the Berea sample saturated by different fluids. The "*experimentally undrained*" model is used for the predictions, with the measured dead volume.

discontinuities (flat geometry at two-grain junctions). The latter type of feature is known to be the major contributor to the observed stress sensitivity of various physical properties such as elastic wave velocities (e.g., Christensen and Wang 1985; Sayers *et al.* 1990; Seipold *et al.* 1998).

The Berea sandstone sample chosen has a porosity of $\phi = 19.3$ % and a permeability of $\kappa \sim 10$ mD (i.e., 10^{-14} m^2). The experimental measurements are similar to that for Fo7 (Pimienta *et al.* 2015a), except that the data for the dry sample have also been obtained under loading conditions. This has been done to discard any possible hysteresis effect (Fig. 9a). The parameters used as model input are essentially very similar to that of Table 1. The sample's length and diameter are the same, and porosity ($\phi = 19.3$ %), permeability ($\kappa = 10^{-14}$ m^2), and drained bulk modulus ($K_d \sim 6.5$ GPa) differ. As for before, ϕ, κ, and K_d are used to calculate the other properties/parameters using the theory of poroelasticity.

"Experimentally undrained" boundary conditions

Again, predictions are made according to the experimental conditions. The 1D model with "*experimentally undrained*" boundary conditions is used, and the "*locally averaged*" K_{la} and $Q_{K_{la}}^{-1}$ and the "*local*" B_l are predicted. The dependence to f^* of the measured and modelled elastic (Fig. 10a, b) and hydraulic (Fig. 10c) responses are compared for an effective pressure of $P_{eff} = 1$ MPa.

At lowest frequencies, the measured K (Fig. 10a) under fluid saturation is much higher than K_d. This is precisely what is predicted by K_{la}. This difference results from the interplay between dead volume's and sample's storage capacity, and is theoretically expected. Although the measurement under water saturation remains higher than the model's predictions, an overall good fit is obtained between measurements and predictions for all properties. As f^* increases, both predicted and measured K slightly increase, by about 2 GPa, to reach the value of K_{ud}. A good fit is observed under glycerine saturation. Because the experimental dead volume V_{meas} is small as compared with the Berea pore volume, the measured dispersion/attenuation is much lower than the one expected in case of the transition from K_d to K_{ud}.

The attenuation is strongly controlled by the dead volume effect. Both measurements and predictions indicate a peak of 0.1 (Fig. 10b). A good fit is also obtained between B^* and predicted B_l (Fig. 10c) at lowest frequencies. The magnitude of the measured B^* is well predicted by the model for both

water and glycerine saturations. Yet, the frequency-dependent variations of the "*local*" prediction are spread out as compared with the measurements. These results further indicate that, even for dead volumes much smaller than the one of the present experiment, the drained/undrained transition may be "*seen*" experimentally for highly porous and compressible rocks.

CONCLUSION

To better understand the experimental conditions involved in the measurement of the drained/undrained transition, a 1D model has been developed by solving analytically the partial derivative equation for pressure diffusion. Different boundary conditions have been analysed. The "*undrained*" and "*drained*" boundary conditions assume that fluid is either locked in or free to flow out of the sample. A more realistic "*experimentally undrained*" boundary condition has been investigated by assuming that a dead volume is present at both ends of the sample. Four properties may be predicted by the model, i.e., the pseudo-Skempton coefficient B^*, the pore pressure phase shift ϕ_{B^*}, the bulk modulus K, and the attenuation Q_K^{-1}.

The 1D model is used to test two main aspects, i.e., the the role of the measuring condition and the role of the dead volume. Interestingly, the frequency range for the drained/undrained transition is expected to strongly differ if the measuring method is global (e.g., linear variable differential transformer) or local (e.g. strain gauge). Furthermore, the position of the local measurement is also expected to play a dominant role. Finally, introducing a dead volume at both sample's ends appears to strongly affect the drained/undrained transition. The measured dispersion/attenuation for this effect are expected to be strongly damped if the dead volume is small in comparison with the rock pore volume. Because it originates from an interplay between dead volume's and sample's storage capacity, this effect increases as the rock's compliance and porosity increases.

Comparison between the model's predictions and measurements on a Fontainebleau and a Berea sandstone shows a good fit and an overall consistency. The rock's storage capacity has an important effect. It could result in a non-negligible attenuation even with a very small dead volume if the storage capacity is high.

ACKNOWLEDGMENTS

This work has been partially supported by Total, under the project FR00007429. The authors wish to thank the two anonymous reviewers for their constructive comments. The first author also wishes to thank Dr. Mathias Delescluse for scientific discussions.

REFERENCES

Adam L., Batzle M. and Brevik I. 2006. Gassmann's fluid substitution and shear modulus variability in carbonates at laboratory seismic and ultrasonic frequencies. *Geophysics***71**, F173–F183.

Adam L., Batzle M., Lewallen K. and van Wijk K. 2009. Seismic wave attenuation in carbonates. *Journal of Geophysical Research* **114**(6).

Adelinet M., Fortin J., Guéguen Y., Schubnel A. and Geoffroy L., 2010. Frequency and fluid effects on elastic properties of basalt: experimental investigations. *Geophysical Research Letters* **37**(2), L02303.

Batzle M.L., Han D.-H. and Hofmann R. 2006. Fluid mobility and frequency-dependent seismic velocity direct measurements. *Geophysics* **71**, N1–N9.

Biot M.A. 1956. Theory of propagation of elastic waves in a fluid-saturated porous solid. I. low-frequency range. *The Journal of the Acoustical Society of America* **28**(2), 168–178.

Bourbie T. and Zinszner B. 1985. Hydraulic and acoustic properties as a function of porosity in fontainebleau sandstone. *Journal of Geophysical Research: Solid Earth* **90**(B13), 11524–11532.

Brace W., Walsh J. and Frangos W. 1968. Permeability of granite under high pressure. *Journal of Geophysical Research* **73**, 2225–2236.

Christensen N. and Wang H. 1985. The influence of pore pressure and confining pressure on dynamic elastic properties of berea sandstone. *Geophysics* **50**(2), 207–213.

Cleary M.P. 1978. Elastic and dynamic response regimes of fluid-impregnated solids with diverse microstructures. *International Journal of Solids and Structures* **14**(10), 795–819.

David E., Brantut N., Schubnel A. and Zimmerman R. 2012. Sliding crack model for nonlinearity and hysteresis in the uniaxial stress -strain curve of rock. *International Journal of Rock Mechanics and Mining Sciences* **52**, 9–17.

David E.C., Fortin J., Schubnel A., Guéguen Y. and Zimmerman R.W. 2013. Laboratory measurements of low- and high-frequency elastic moduli in fontainebleau sandstone. *Geophysics* **78**, D369–D379.

Detournay E. and Cheng A.H.-D. 1993. *Fundamentals of Poroelasticity, Vol. 2: Analysis and Design Method*, pp. 113–171. Pergamon Press.

Dunn K.-J. 1986. Acoustic attenuation in fluid-saturated porous cylinders at low frequencies. *The Journal of the Acoustical Society of America* **79**(6), 1709–1721.

Dunn K.-J. 1987. Sample boundary effect in acoustic attenuation of fluid-saturated porous cylinders. *The Journal of the Acoustical Society of America* **81**(5), 1259–1266.

Fortin J., Pimienta L., Guéguen Y., Schubnel A., David E. and Adelinet M. 2014. Experimental results on the combined effects of frequency and pressure on the dispersion of elastic waves in porous rocks. *The Leading Edge* **33**, 648–654.

Ghabezloo S. and Sulem J. 2009. Stress dependent thermal pressurization of a fluid saturated rock. *Rock Mechanics and Rock Engineering* **42**, 1–24.

Ghabezloo S. and Sulem J. 2010. Effect of the volume of the drainage system on the measurement of undrained thermo-poro-elastic parameters. *International Journal of Rock Mechanics and Mining Sciences* **47**, 60–68.

Guéguen Y. and Bouteca M. 2004. *Mechanics of Fluid-Saturated Rocks, Vol. 89*. Academic Press.

Hsieh P.A., Tracy J.V., Neuzil C.E, Bredehoeft J.D. and Silliman S.E. 1981. A transient laboratory method for determining the hydraulic properties of tight rocks –I. theory. *International Journal of Rock Mechanics and Mining Sciences & Geomechanics Abstracts* **18**(3), 245–252.

O'Connell R.J. and Budiansky B. 1974. Seismic velocities in dry and saturated cracked solids. *Journal of Geophysical Research* **79**, 5412–5426.

Paffenholz J. and Burkhardt H. 1989. Absorption and modulus measurements in the seismic frequency and strain range on partially saturated sedimentary rocks. *Journal of Geophysical Research: Solid Earth* **94**, 9493–9507.

Pimienta L., Fortin J. and Guéeguen 2014a. Evidence of a drained to undrained frequency dependent transition from elastic and hydraulic diffusion properties on a Fontainebleau sandstone. In: *Proceedings of the 84th SEG Annual Meeting*, pp. 2969–2972.

Pimienta L., Fortin J. and Guéguen Y. 2014b. Investigation of elastic weakening in limestone and sandstone samples from moisture adsorption. *Geophysical Journal International* **199**, 335–347.

Pimienta L., Fortin J. and Guéguen Y. 2015a. Bulk modulus dispersion and attenuation in sandstones. *Geophysics* **80**, D111–D127.

Pimienta L., Fortin J. and Guéguen Y. 2015b. Experimental study of Young's modulus dispersion and attenuation in fully saturated sandstones. *Geophysics* **80**(5), L57–L72.

Pimienta L., Fortin J. and Guéguen Y. 2016. Effect of fluids and frequencies on Poisson's ratio of sandstone samples. *Geophysics* **81**(2), in press.

Pimienta L., Sarout J., Esteban L., and Delle Piane C. 2014c. Prediction of rocks thermal conductivity from elastic wave velocities, mineralogy and microstructure. *Geophysical Journal International* **197**(2), 860–874.

Jackson I. and Paterson M. 1987. Shear modulus and internal friction of calcite rocks at seismic frequencies: pressure, frequency and grain size dependence. *Physics of the Earth and Planetary Interiors* **45**, 349–367.

Kümpel H.-J. 1991. Poroelasticity: parameters reviewed. *Geophysical Journal International* **105**, 783–799.

Lienert B.R. and Manghnani M.H. 1990. The relationship between $Q^{-1}E$ and dispersion in extensional modulus E. *Geophysical Research Letters* **17**, 677–680.

Lin W. 1977. *Compressible Fluid Flow Through Rocks of Variable Permeability. Technical Report, California Univ., Livermore (USA). Lawrence Livermore Lab*.

Madonna C. and Tisato N. 2013. A new seismic wave attenuation module to experimentally measure low-frequency attenuation in extensional mode. *Geophysical Prospecting* **61**, 302–314.

Mikhaltsevitch V., Lebedev M. and Gurevich B. 2014. A laboratory study of low-frequency wave dispersion and attenuation in water-saturated sandstones. *The Leading Edge* **33**, 616–622.

Rice J.R. and Cleary M.P. 1976. Some basic stress diffusion solutions for fluid-saturated elastic porous media with compressible constituents. *Reviews of Geophysics* **14**, 227–241.

Sayers C., Van Munster, J. and King M. 1990. Stress-induced ultrasonic anisotropy in Berea sandstone. *International Journal of Rock Mechanics and Mining Sciences & Geomechanics Abstracts* **27**(5), 429–436.

Seipold U., Mueller H. and Tuisku P. 1998. Principle differences in the pressure dependence of thermal and elastic properties of crystalline rocks. *Physics and Chemistry of the Earth* **23**, 357–360.

Song I. and Renner J. 2006. Linear pressurization method for determining hydraulic permeability and specific storage of a rock sample. *Geophysical Journal International* **27**(164), 685–696.

Song I. and Renner J. 2007. Analysis of oscillatory fluid flow through rock samples. *Geophysical Journal International* **170**, 195–204.

Subramaniyan S., Quintal B., Tisato N., Saenger E.H. and Madonna C. 2014. An overview of laboratory apparatuses to measure seismic attenuation in reservoir rocks: *Geophysical Prospecting* **62**(6), 1211–1223.

Takei Y., Fujisawa K. and McCarthy C. 2011. Experimental study of attenuation and dispersion over a broad frequency range: 1. the apparatus. *Journal of Geophysical Research: Solid Earth* **116**(B9).

Tisato N. and Madonna C. 2012. Attenuation at low seismic frequencies in partially saturated rocks. Measurements and description of a new apparatus. *Journal of Applied Geophysics* **86**, 44–53.

Wang H.F. 2000. *Theory of Linear Poroelasticity: Princeton Series in Geophysics*. Princeton University Press, Princeton, NJ.

Winkler K. and Nur A. 1979. Pore fluids and seismic attenuation in rocks. *Geophysical Research Letters* **6**, 1–4.

Zimmerman R. 2000. Coupling in poroelasticity and thermoelasticity. *International Journal of Rock Mechanics and Mining Sciences* **37**, 79–87.

Author Query Form

Journal **GPR**

Article **gpr12390**

Dear Author

During the copy-editing of your paper, the following queries arose. Please respond to these by marking up your proofs with the necessary changes/additions. Please write your answers clearly on the query sheet if there is insufficient space on the page proofs. If returning the proof by fax do not write too close to the paper's edge. Please remember that illegible mark-ups may delay publication.

Query No.	Description	Remarks
Q1	Author: Please confirm that given names (red) and surnames/family names (green) have been identified correctly.	
Q2	Author: Prasad and Manghnani (1997) is not in the reference list. Please supply full source info there, or remove this in-text citation.	

USING e-ANNOTATION TOOLS FOR ELECTRONIC PROOF CORRECTION

Required software to e-Annotate PDFs: Adobe Acrobat Professional or Adobe Reader (version 9.0 or above). (Note that this document uses screenshots from Adobe Reader X)
The latest version of Acrobat Reader can be downloaded for free at: http://get.adobe.com/reader/

Once you have Acrobat Reader open on your computer, click on the Comment tab at the right of the toolbar:

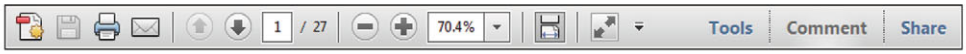

This will open up a panel down the right side of the document. The majority of tools you will use for annotating your proof will be in the Annotations section, pictured opposite. We've picked out some of these tools below:

1. Replace (Ins) Tool – for replacing text.

Strikes a line through text and opens up a text box where replacement text can be entered.

How to use it

- Highlight a word or sentence.
- Click on the Replace (Ins) icon in the Annotations section.
- Type the replacement text into the blue box that appears.

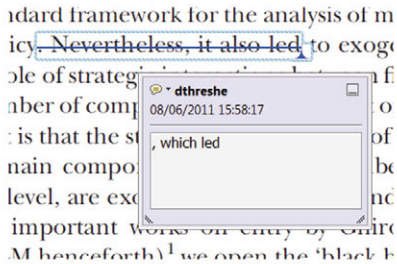

2. Strikethrough (Del) Tool – for deleting text.

Strikes a red line through text that is to be deleted.

How to use it

- Highlight a word or sentence.
- Click on the Strikethrough (Del) icon in the Annotations section.

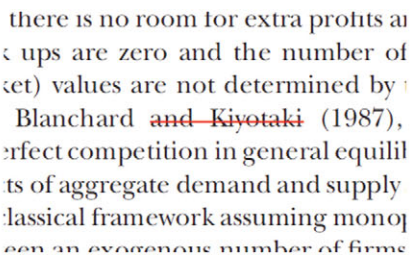

3. Add note to text Tool – for highlighting a section to be changed to bold or italic.

Highlights text in yellow and opens up a text box where comments can be entered.

How to use it

- Highlight the relevant section of text.
- Click on the Add note to text icon in the Annotations section.
- Type instruction on what should be changed regarding the text into the yellow box that appears.

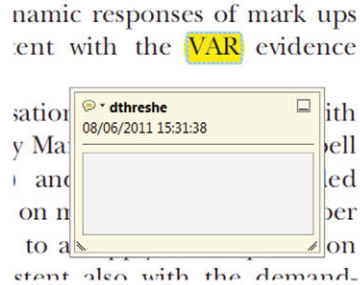

4. Add sticky note Tool – for making notes at specific points in the text.

Marks a point in the proof where a comment needs to be highlighted.

How to use it

- Click on the Add sticky note icon in the Annotations section.
- Click at the point in the proof where the comment should be inserted.
- Type the comment into the yellow box that appears.

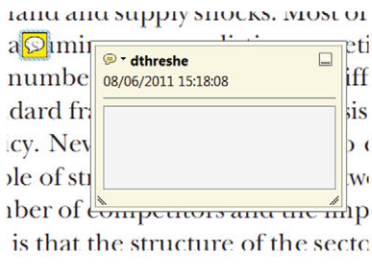

USING e-ANNOTATION TOOLS FOR ELECTRONIC PROOF CORRECTION

5. Attach File Tool – for inserting large amounts of text or replacement figures.

Inserts an icon linking to the attached file in the appropriate pace in the text.

How to use it

- Click on the Attach File icon in the Annotations section.
- Click on the proof to where you'd like the attached file to be linked.
- Select the file to be attached from your computer or network.
- Select the colour and type of icon that will appear in the proof. Click OK.

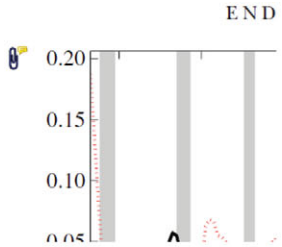

6. Add stamp Tool – for approving a proof if no corrections are required.

Inserts a selected stamp onto an appropriate place in the proof.

How to use it

- Click on the Add stamp icon in the Annotations section.
- Select the stamp you want to use. (The Approved stamp is usually available directly in the menu that appears).
- Click on the proof where you'd like the stamp to appear. (Where a proof is to be approved as it is, this would normally be on the first page).

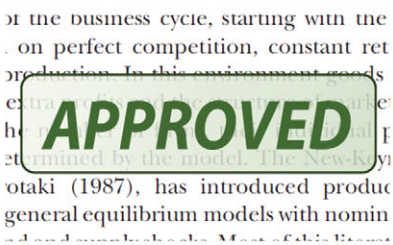

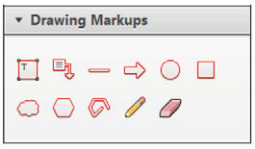

7. Drawing Markups Tools – for drawing shapes, lines and freeform annotations on proofs and commenting on these marks.

Allows shapes, lines and freeform annotations to be drawn on proofs and for comment to be made on these marks..

How to use it

- Click on one of the shapes in the Drawing Markups section.
- Click on the proof at the relevant point and draw the selected shape with the cursor.
- To add a comment to the drawn shape, move the cursor over the shape until an arrowhead appears.
- Double click on the shape and type any text in the red box that appears.

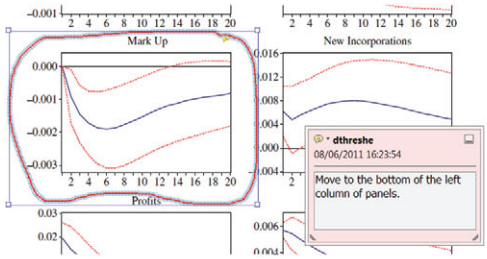

For further information on how to annotate proofs, click on the Help menu to reveal a list of further options: